Available online at www.sciencedirect.com
ScienceDirect
Journal of Nuclear Materials 363–365 (2007) 294–300
journal of nuclear materials
www.elsevier.com/locate/jnucmat

Divertor transport study in the large helical device

M. Kobayashi [a,*], Y. Feng [b], S. Masuzaki [a], M. Shoji [a], J. Miyazawa [a], T. Morisaki [a], N. Ohyabu [a], N. Ashikawa [a], A. Komori [a], O. Motojima [a], The LHD Experimental Group [a], Y. Igitkhanov [b], F. Sardei [b], D. Reiter [c]

[a] National Institute for Fusion Science, Oroshi-cho 322-6, Toki 509-5292, Japan
[b] Max-Planck-Institut fuer Plasmaphysik, Teilinstitut Greifswald, Euratom Association, 17491 Greifswald, Germany
[c] Institut fuer Plasmaphysik, Forschungszentrum Juelich GmbH, 52425 Juelich, Germany

Abstract

The edge transport properties in LHD have been investigated in order to clarify divertor/SOL functions of heliotron type device. The momentum loss, mainly through friction of counter-flows induced by ergodic field lines, breaks the pressure conservation along flux tubes. This prevents high recycling regime even at high density operation, $\bar{n} \sim 7 \times 10^{19}\ \mathrm{m}^{-3}$. The momentum loss is found to be larger than in W7-AS. This is because of the higher ratio of perpendicular and parallel transport scale length, $\sim 10^{-4}$, in the ergodic layer, which enhances the friction between counter-flows more than in the island divertor. In the heliotron configuration, a large temperature drop from LCFS to divertor by an order of magnitude is easily realized due to the long connection length in the ergodic layer. This is certainly a favourable feature for future reactors in terms of reduction of damage on the divertor plate.

PACS: 52.55.Hc; 52.55.Rk; 52.25.Fi; 52.65.Pp

Keywords: LHD; 3D Edge plasma; Edge modelling; Stochastic boundary

1. Introduction

The large helical device (LHD) is a heliotron type machine, which has been built to explore more reactor relevant operational regimes and to demonstrate an attractive feature of a stellarator [1]. The most remarkable is the recent progress both of the core plasma performance with more than 4% of beta [2] and the steady state operation with more than one hour [3] and with an input energy of 1.3 GJ [4]. As the core plasma energy content and also the operation duration increase, control of edge plasma transport has become more critical in order to protect the core plasma from an impurity contamination and the plasma facing materials from excessive heat load as well.

LHD is installed with the helical divertor, which can operate with different magnetic axis positions (R_{ax}). Its feasibility and the physics of the transport process are, however, not yet fully identified.

* Corresponding author. Fax: +81 572 58 2618.
E-mail address: kobayashi.masahiro@LHD.nifs.ac.jp (M. Kobayashi).

0022-3115/$ - see front matter © 2007 Elsevier B.V. All rights reserved.
doi:10.1016/j.jnucmat.2007.01.038

Different from the poloidal divertor configuration of tokamaks, the magnetic field structure in the edge region consists of the island overlapping region, ergodic layer and divertor legs. This geometrical significance is strongly affecting the edge transport process and requires modifications of the transport picture already developed in tokamaks.

In this paper, the edge transport properties in LHD are analyzed for characterising divertor/SOL function in the heliotron type configuration. Poincare plot of the field line tracing for the configuration of R_{ax} (magnetic axis) = 3.75 m in LHD is shown in Fig. 1. The closed flux surfaces are surrounded by ergodic layer of thickness of several to 20 cm, which is created by intrinsically existing magnetic islands at the periphery. The connection length L_C in the ergodic layer is of order of kilometers, and the field lines are connected to the divertor plates through divertor legs. Because of the strong poloidal magnetic component at the legs, the length of the magnetic field lines from X-point to the plates is only ~2 m.

As shown in the divertor transport study in W7-AS, the cross field transport starts to play an important role in the islands divertor region [5], which has larger connection length and shorter divertor-to-core distances, compared to tokamaks. In view of the ratio of L_C to the width of the ergodic layer, such condition could be achieved in LHD as well, whereas in the divertor legs, parallel transport will be dominant like in tokamaks. The experimental data shows no evidence of high recycling in LHD [6], which is similar to the observation in W7-AS. From the next section, the detailed analysis is presented.

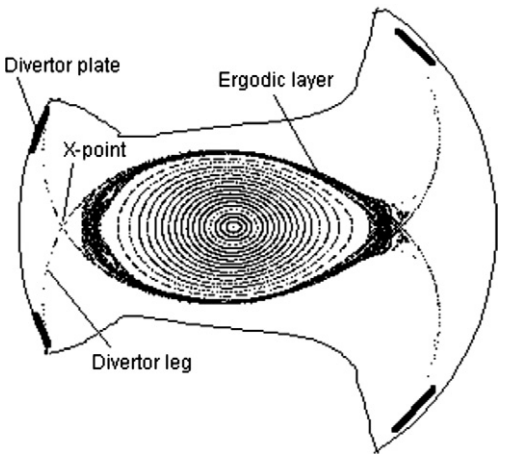

Fig. 1. Poincare plot of field line tracing for the configuration of $R_{ax} = 3.75$ m.

2. Transport in divertor legs

Since the parallel transport is dominating at the divertor legs because of the short length, the standard two-point model used in tokamaks can be applied. The bolometer measurement, which is calibrated to estimate radiated power in the whole torus, gives a radiation fraction of 10–20% of total deposited power for the typical LHD shots. On the other hand, the CCD camera shows that most of the radiation is located at the ergodic layer, which is upstream of the divertor legs. We, therefore, neglect the energy loss due to the radiation along the divertor legs. The energy conduction in parallel direction is given by

$$q_{\|\mathrm{cond}} = -\kappa_0 T^{5/2} \frac{\mathrm{d}T}{\mathrm{d}l}, \tag{1}$$

where l is the distance along the legs measured from upstream. Integrating from X-point to divertor plate, it gives

$$T_{\mathrm{div}}^{7/2} = T_{\mathrm{X}}^{7/2} - \frac{7}{2}\frac{q_{\|\mathrm{cond}} L_C}{\kappa_0}. \tag{2}$$

From Bohm condition at the divertor plate, $q_{\|\mathrm{cond}}$ is

$$q_{\|\mathrm{cond}} = f_{\mathrm{cond}} \gamma T_{\mathrm{div}} n_{\mathrm{div}} c_{\mathrm{sd}}, \tag{3}$$

where f_{cond} is a fraction of conduction, i.e. $f_{\mathrm{cond}} = q_{\|\mathrm{cond}}/q_{\|\mathrm{total}}$, ranging from 0 to 1. The measurements of CCD camera and the neutral transport simulation show that there is substantial amount of H_α radiation at ergodic layer [7], which gives a certain amount of convection energy. We set thus $f_{\mathrm{cond}} = 0.5$. Eqs. (2) and (3) are combined to

$$T_{\mathrm{div}}^2 = \frac{n_{\mathrm{div}} L_C f_{\mathrm{cond}}}{C_1 (f_{\mathrm{T}}^{7/2} - 1)}, \tag{4}$$

where $f_{\mathrm{T}} = T_{\mathrm{X}}/T_{\mathrm{div}}$, $C_1 = \frac{2\kappa_0 m_i^{1/2}}{7\gamma e^{3/2}} \approx 5.2 \times 10^{16} (\mathrm{m^{-2}\,eV^{-2}})$ and $L_C = 2$ m. Eq. (4) is plotted in Fig. 2 for different values of f_{T} together with experimental data of n_{div} and T_{div} measured by Langmuir probes at the divertor plate for typical operation range in LHD, i.e. line averaged density $\bar{n}_e = 3 \sim 8 \times 10^{19}\,\mathrm{m^{-3}}$ and input power = 4–5 MW. It is seen that most of the data is located at the region $T_{\mathrm{X}}/T_{\mathrm{div}} < 1.5$. The analysis indicates that there is almost no temperature gradient along divertor legs. This is attributed to the rather short parallel distance from X-point to

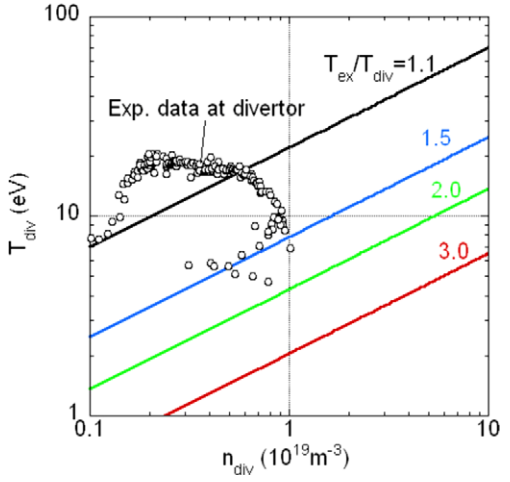

Fig. 2. Plot of Eq. (4) in $n_{\rm div} - T_{\rm div}$ space for different $f_{\rm T} = T_{\rm X}/T_{\rm div}$. Open circles are experimental data of $n_{\rm div}$ and $T_{\rm div}$ at the divertor plates.

divertor plates and also to the open divertor structure, which cannot keep recycling neutrals and impurity near the target for radiating and reducing $T_{\rm div}$. This also explains the low density at the divertor, i.e. $n_{\rm div} \leqslant 1 \times 10^{19}\ {\rm m}^{-3}$ as shown in the figure.

3. Transport in ergodic layer

3.1. $\perp$ vs. $\parallel$ energy transport

In the ergodic layer, collisionality is high, i.e. $L_{\rm C}/\lambda_{\rm ee} = L_{\rm C} n/(10^{16} T_{\rm e}^2) \approx 100$ with $n \sim 10^{19}\ {\rm m}^{-3}$ and $T_{\rm e} \sim 100$ eV. It can thus be assumed that there is a significant temperature drop along flux tubes (this is confirmed later by the experimental data in Section 3.2). Similarly to Eqs. (1) and (2) but for uniformly distributed energy input along flux tubes, parallel energy flux is given by

$$q_{\parallel} = \frac{4}{7}\frac{\kappa_0 T_{\rm u}^{7/2}}{L_{\rm C}/2}, \tag{5}$$

with an assumption that $T_{\rm div}^{7/2} \ll T_{\rm u}^{7/2}$, where $T_{\rm u}$ is a temperature at upstream (near LCFS). Using Eq. (5), the energy transport time along flux tubes is then expressed as

$$\tau_{\rm E\parallel} = \frac{3 n_{\rm u} T_{\rm u} L_{\rm C}}{2 q_{\parallel}} = \frac{21 n_{\rm u} L_{\rm C}^2}{16 \kappa_0 T_{\rm u}^{5/2}}. \tag{6}$$

On the other hand, the energy transport time in perpendicular direction in ergodic layer could be given as

$$\tau_{\rm E\perp} = \frac{\Delta x^2}{2\chi_{\perp}}, \tag{7}$$

where Δx and $\chi_{\perp}$ are radial thickness of the ergodic layer and perpendicular heat conductivity, respectively. For $\Delta x =$ several cm and $\chi_{\perp} = 1.0\ {\rm m}^2/{\rm s}$ (assumed to be anomalous), $\tau_{\rm E\perp} = 1$–5 ms. $\tau_{\rm E\parallel}$ is plotted in Fig. 3 as a function of $L_{\rm C}$ for different temperatures together with the range of $\tau_{\rm E\perp}$. It is found that in the range of $100 < L_{\rm C} < 1000$ m, the parallel energy transport time is comparable with the perpendicular one, i.e. $\tau_{\rm E\parallel} \sim \tau_{\rm E\perp}$, on the other hand at $L_{\rm C} \gg 1000$ m the perpendicular transport dominates, $\tau_{\rm E\parallel} \gg \tau_{\rm E\perp}$, which corresponds to a confinement region.

Fig. 4(a) and (b) shows radial profile of $L_{\rm C}$ and electron pressure measured by Thomson scattering system at the outer midplane, respectively. It is clearly seen that around $R = 4.6$ m, where $L_{\rm C}$ becomes lower than 1000 m, the slope of pressure changes, indicating change of transport characteristic. The similar behaviour of electron pressure or electron temperature (i.e. steepening around the boundary of ergodic layer) was observed in TEXT [8], Tore Supra [9] and DIII-D [10]. Although, to date, several models have been proposed for explaining the steepening [11,12], it is not very clear at the moment which model is appropriate and the detailed discussion on this topic is beyond the scope of the present analysis.

3.2. Effect of cross field transport

In order to analyze the transport in ergodic layer, the 3D edge transport code, EMC3–EIRENE [13,14], has been implemented on the configuration. Fig. 5(a) and (b) shows the electron temperature

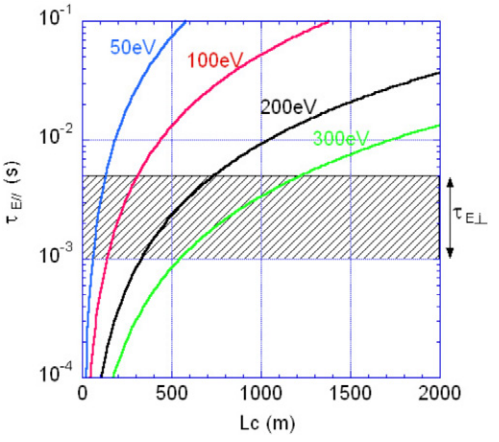

Fig. 3. Parallel energy transport time $\tau_{\rm E\parallel}$, Eq. (6), as a function of $L_{\rm C}$ for different $T_{\rm u}$'s. The range of perpendicular transport time $\tau_{\rm E\perp}$ is also indicated.

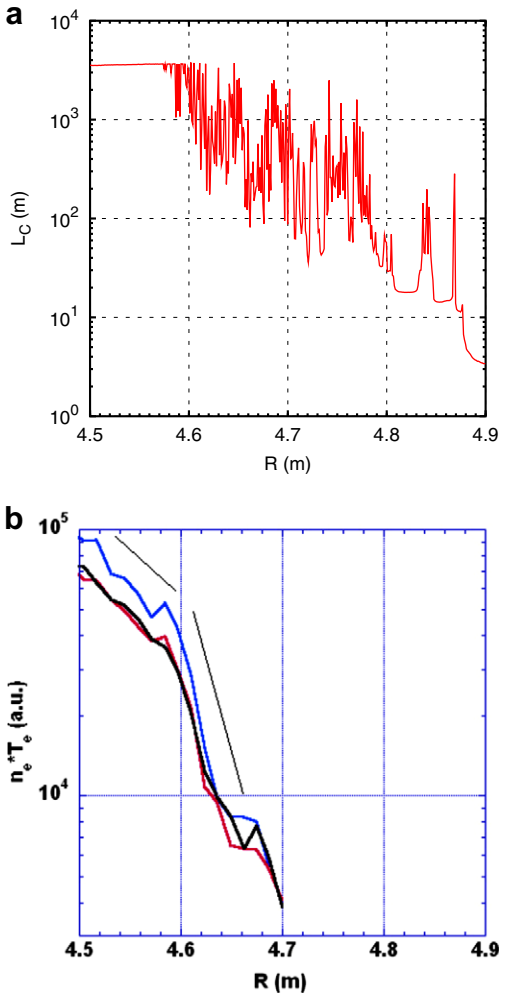

Fig. 4. Radial profile of (a) L_C, which is calculated up to 150 toroidal turns (~3500 m) and (b) electron pressure at the outer midplane for $R_{ax} = 3.75$ m. The pressure was measured by the Thomson scattering system.

profile on poloidal plane obtained by the 3D modelling, together with L_C profile, respectively, for the case of $R_{ax} = 3.75$ m, $n_u = 2 \times 10^{19}$ m^{-3}, $\chi_\perp = 0.6$ m^2/s, $D_\perp = 0.3$ m^2/s, where the power flow to the SOL, P_{SOL}, is 4 MW. L_C is resolved up to 10 km, plotted in logarithmic scale. The pattern of long L_C region is clearly reflected on the T_e profile, appearing as high temperature. This means an energy flow channel through long flux tubes, which penetrate closer to LCFS. The radial T_e profile measured by the Thomson scattering system is in good agreement with the 3D code result, as shown in Fig. 5(c), e.g. the decrease at $R = 2.78$ m due to short L_C region and the flattening at $R = 2.87$ m caused by the island.

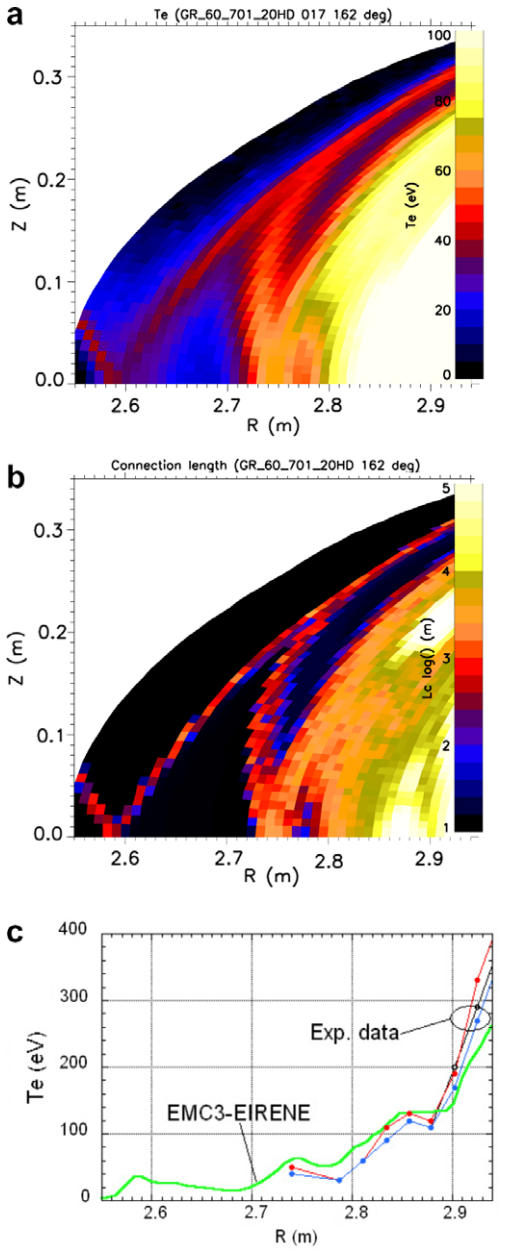

Fig. 5. (a) T_e profile in poloidal plane obtained by EMC3–EIRENE for the case of $R_{ax} = 3.75$ m, $n_u = 2 \times 10^{19}$ m^{-3}, $\chi_\perp = 0.6$ m^2/s, $D_\perp = 0.3$ m^2/s and $P_{SOL} = 4$ MW. T_e is resolved up to 100 eV. (b) L_C profile in poloidal plane. (c) Radial profiles of T_e at inner midplane obtained from EMC3–EIRENE and the experiments for $\bar{n}_e \sim 2 \times 10^{19}$ m^{-3} and input power ~4 MW.

Fig. 6(a) and (b) shows the upstream (near LCFS) and divertor plasma parameter as a function of $\bar{n}_e$, together with the 3D modelling results. For the present analysis, impurity transport and impurity radiation were not taken into account. The

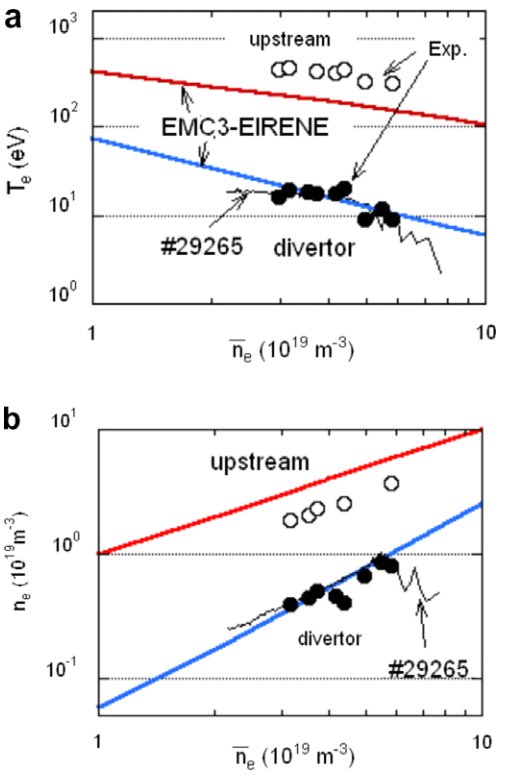

Fig. 6. Dependence of plasma parameters at upstream (near LCFS) and divertor on $\bar{n}_e$, obtained from EMC3–EIRENE and experiments.

modelling are in reasonable agreement with the experiments except around $\bar{n}_e \geqslant 7 \times 10^{19}$ m^{-3}, where both temperature and density at the divertor start to decrease, followed by a radiation collapse. It is remarkable that T_e decreases from several hundreds eV at upstream down to a few tens eV at divertor, i.e. by an order of magnitude. Nevertheless, n_{div} never exceeds n_u, and there is no evidence of a high recycling regime like $n_{div} \propto n_u^3$ and $T_{div} \propto n_u^{-2}$. It should be noted that the present 3D modelling does not include impurity transport, so that the significant temperature drop across the ergodic layer is not due to the radiation loss.

In order to elucidate the reason for an absence of high recycling behaviour, we introduce cross field transport effect, which was shown to be comparable with parallel transport in ergodic layer in Section 3.1. The extended two-point model with cross field terms [5] is derived as follows. In the ergodic layer, ratio of cross field and parallel transport scale length is defined as $\beta \equiv \Delta x/L_C$. The energy (electron plus ion) and momentum transport equations in radial direction are

$$\beta \frac{d}{dx}\left(-\kappa_0 T^{5/2} \beta \frac{dT}{dx}\right) + \frac{d}{dx}\left(-\chi_\perp n \frac{dT}{dx}\right) = 0, \quad (8)$$

$$\beta \frac{d}{dx}\left(mnV_\parallel^2 + p\right) = -D_\perp \frac{mn\Delta V_\parallel}{\Delta^2}, \quad (9)$$

where it is assumed that $T_e = T_i = T$ and energy source/sink due to interaction with neutrals or impurity is negligible. The first terms in Eqs. (8) and (9) represent projection of the parallel transport onto the radial direction, x, due to the stochastic field lines. The right hand side of Eq. (9) is accounting for a momentum loss in perpendicular direction. Especially in the ergodic layer, this term becomes important because of friction between the counter-flows which are induced by the ergodic field lines, as found in the 3D modelling. Fig. 7 shows Mach number profile in poloidal plane, where yellow and dark blue colour indicate flows in positive and negative direction of toroidal angle, respectively. In Eq. (9), $\Delta V_\parallel$ and Δ are the relative velocity of two neighbouring flows and the characteristic distance between the flow channels. The boundary condition at the down stream for energy flux is given by

$$q_\parallel = \gamma n_d T_d c_{sd}, \quad (10)$$

while for $V_\parallel$, $V_\parallel = c_{sd}$ at downstream and $V_\parallel = 0$ at upstream, respectively. Integrating the Eqs. (8) and (9) from upstream to downstream, the extended

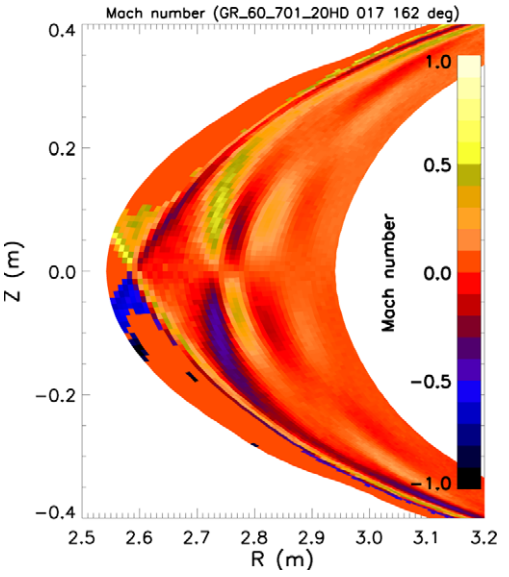

Fig. 7. Mach number profile in poloidal plane obtained by EMC3–EIRENE. The yellow and dark blue colour represent parallel flow in positive and negative toroidal direction. (For interpretation of the references to color in this figure legend, the reader is referred to the web version of this article.)

two-point model with cross field terms is obtained as

$$T_u^{7/2} = T_d^{7/2} + \frac{7q_{\parallel}L_C}{2\kappa_0} - \frac{7\chi_{\perp}n_u}{2\beta^2\kappa_0}(T_u - T_d), \quad (11)$$

$$p_u = 2p_d(1 + f_m), \quad (12)$$

where f_m is a momentum loss factor,

$$f_m = \frac{D_{\perp}}{\beta c_{sd}}\left(\frac{1}{c_{sd}n_d}\int \frac{n\Delta V_{\parallel}}{\Delta^2}\,dx\right). \quad (13)$$

When $\beta \to \infty$, the third term on the right hand side of Eq. (11) and f_m vanish, and the model becomes the standard two-point model in tokamaks.

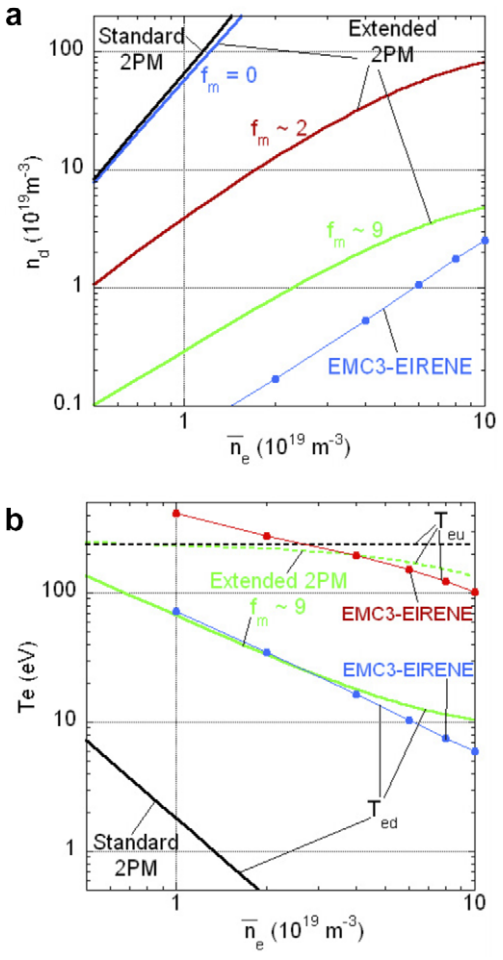

Fig. 8. Solution of the extended two-point model, Eqs. (10)–(13), together with the 3D results: (a) downstream density n_d, (b) solid lines for T_d, broken lines for T_u. Black: standard 2PM, blue: extended 2PM with $f_m = 0$, red: extended 2PM with $f_m \sim 2$, green: extended 2PM with $f_m \sim 9$. The results of EMC3–EIRENE are indicated by lines with circles. (For interpretation of the references to color in this figure legend, the reader is referred to the web version of this article.)

The results are plotted in Fig. 8 for different f_m's, together with the solution obtained by EMC3–EIRENE. Without the cross field terms, the solution shows high recycling behaviour, i.e. $n_d \propto n_u^3$ and $T_d \propto n_u^{-2}$, which is largely different from the 3D results. By increasing f_m and enhancing the momentum loss, the extended two-point model results approach the 3D code ones. It indicates that the large momentum loss, $f_m \sim 9$ i.e. an order of magnitude, suppresses the density increase at downstream, preventing high recycling regime. Compared to the analysis in W7-AS [5], it seems that the momentum loss is larger in LHD. This is because of the smaller $\beta \sim 10^{-4}$, which is $\sim 10^{-3}$ in W7-AS, and the friction between counter-flows scattered in the ergodic layer as shown in Fig. 7. From Eq. (11), it is seen that the large drop of the temperature from LCFS to divertor is due to the long L_C in the ergodic layer, compared to other machines. This is a big advantage of the heliotron configuration, where the ergodic layer intrinsically exists at the periphery without additional perturbation coils.

When the density is increased further, $\bar{n} \sim 10^{20}$ m^{-3}, it was observed that the ion saturation current at the divertor starts to decrease by a factor of 10, and the fraction of impurity radiation reaches 50% of the total input power [15]. The radiation belt is found to locate around LCFS and rotating in toroidal and poloidal direction. This could be called detachment in the sense that the plasma flux to the divertor significantly decrease. The mechanism of the detachment is under investigation.

4. Conclusions

The edge transport properties in LHD have been analyzed in order to clarify the divertor/SOL function of the heliotron type device. The results of the analysis are summarized as follows:

1. The analysis of n_{div} and T_{div} measured by Langmuir probes shows that at the divertor legs, no significant temperature drop is expected from X-point to divertor plates. This also means no significant density rise at the divertor plates. Therefore, along the divertor legs, the plasma parameters does not change significantly.
2. In the ergodic layer, at the region of $L_C = 100$–1000 m, the parallel energy transport time becomes the same order of magnitude as the perpendicular one, i.e. $\tau_{E\parallel} \sim \tau_{E\perp}$. The electron pressure profile changes its gradient from the

confinement region ($\tau_{E\parallel} \gg \tau_{E\perp}$) to the intermediate region ($\tau_{E\parallel} \sim \tau_{E\perp}$), indicating change of transport characteristics between the two regions.

3. The momentum loss, mainly through the friction of counter-flows induced by the ergodic field lines, breaks the pressure conservation along flux tubes. This moderate the density rise (temperature drop) at the divertor, resulting in no high recycling regime even at high density operation, $\bar{n} \sim 7 \times 10^{19}$ m^{-3}. The momentum loss is found to be higher than the case of W7-AS. This is because of the higher ratio of perpendicular and parallel transport scale, $\beta \sim 10^{-4}$, and of the ergodic layer, which enhances the friction between counter-flows more than in the island divertor.
4. In the heliotron configuration, a large temperature drop from LCFS to divertor by an order of magnitude, is easily realized due to the long L_C in the ergodic layer, even without high recycling regime. This is certainly a favourable feature for future reactors in terms of reduction of damage at the divertor plate. For an improvement of pumping efficiency, on the other hand, a closed divertor system is being considered as a potential solution.

Acknowledgements

This work was financially supported by NIFS06ULPP530 and NIFS05ULPP530.

References

[1] N. Ohyabu et al., Nucl. Fusion 34 (1994) 387.
[2] A. Komori et al., Phys. Plasmas 12 (2005) 056122;
S. Sakakibara et al., Fusion Sci. Technol. 50 (2006) 177.
[3] T. Seki et al., Fus. Technol. 40 (2001) 253.
[4] R. Kumazawa et al., Nucl. Fusion 46 (2006) S13.
[5] Y. Feng et al., Nucl. Fusion 46 (2006) 807.
[6] S. Masuzaki et al., Nucl. Fusion 42 (2002) 750;
S. Masuzaki et al., J. Nucl. Mater. 313–316 (2003) 852.
[7] M. Shoji et al., these Proceedings.
[8] T.E. Evans et al., J. Nucl. Mater. 145–147 (1987) 812.
[9] Ph. Ghendrih et al., Nucl. Fusion 42 (2002) 1221.
[10] I. Joseph et al., these Proceedings.
[11] S. Feron et al., J. Nucl. Mater. 241–243 (1997) 328.
[12] A.H. Boozer, Phys. Plasmas 12 (2005) 092504.
[13] Y. Feng et al., Contribution Plasma Phys. 44 (2004) 57.
[14] D. Reiter et al., Fusion Sci. Technol. 47 (2005) 172, www.eirene.de (2004).
[15] J. Miyazawa et al., Nucl. Fusion 46 (2006) 532.